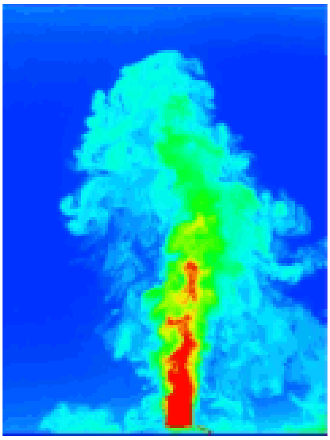

Journal of Turbulence
Publication details, including instructions for authors and subscription information:
http://www.tandfonline.com/loi/tjot20

Acceleration in turbulent channel flow

L. Chen [a], S. W. Coleman [a], J. C. Vassilicos [a] & Z. Hu [b]

[a] Department of Aeronautics and Institute of Mathematical Sciences, Imperial College London, London, SW7 2AZ, UK

[b] Aeronautics and Astronautics, School of Engineering Sciences, University of Southampton, Highfield, Southampton, SO17 1BJ, UK

Published online: 01 Oct 2010.

To cite this article: L. Chen, S. W. Coleman, J. C. Vassilicos & Z. Hu (2010) Acceleration in turbulent channel flow, Journal of Turbulence, 11, N41, DOI: 10.1080/14685248.2010.510842

To link to this article: http://dx.doi.org/10.1080/14685248.2010.510842

Journal of Turbulence
Vol. 11, No. 41, 2010, 1–23

Taylor & Francis
Taylor & Francis Group

Acceleration in turbulent channel flow

L. Chen[a], S. W. Coleman[a], J. C. Vassilicos[a*] and Z. Hu[b]

[a]*Department of Aeronautics and Institute of Mathematical Sciences, Imperial College London, London, SW7 2AZ, UK;* [b]*Aeronautics and Astronautics, School of Engineering Sciences, University of Southampton, Highfield, Southampton, SO17 1BJ, UK*

(*Received 15 January 2010; final version received 17 July 2010*)

We use Direct Numerical Simulations of turbulent channel flow to study the acceleration $\boldsymbol{A}$ corresponding to the full fluid velocity $\boldsymbol{u}$ and the acceleration $\boldsymbol{a}$ corresponding to the fluctuating velocity $\boldsymbol{u}' \equiv \boldsymbol{u} - \langle \boldsymbol{u} \rangle$, where $\langle \boldsymbol{u} \rangle$ is the mean flow. The mean acceleration $\langle \boldsymbol{A} \rangle = \langle \boldsymbol{a} \rangle$ is not zero, and the fluctuations of the convective and local parts of $\langle \boldsymbol{A} \rangle$ around their means approximately cancel in the intermediate log-like layer. The motions of stagnation points where $\boldsymbol{u}' = 0$ are controlled by $\boldsymbol{a}$. In this intermediate layer, the fluctuations of $\boldsymbol{a}$ around its mean predominantly come from the fluctuations of its local part. Stagnation points move with an average velocity, which equals the average fluid velocity at these points. The fluctuations around this average stagnation point motion decrease in the log-like layer with increasing distance from the wall.

1. Introduction

It is well known (e.g. [1]) that, in turbulent channel flows, for example, as the Reynolds number increases to infinity, the ratio of the channel width h to the wall unit distance δ_ν also increases to infinity. As a result, an intermediate range of distances z from the channel walls forms where $\delta_\nu \ll z \ll h/2$. Stripped to its bare essentials, the main assumption behind the intermediate asymptotics that lead to the form of the mean velocity profile in this intermediate range is this: As the Reynolds number tends to infinity, *something* is asymptotically independent of both h and the fluid's kinematic viscosity ν in this intermediate range. This *something* is usually taken to be the mean shear $\frac{d}{dz}U$ (where U is the mean flow velocity and z is the wall-normal coordinate). In this case, the immediate consequence of the intermediate asymptotic assumption is that in the intermediate range $\delta_\nu \ll z \ll h/2$,

$$\frac{d}{dz}U \approx \frac{u_\tau}{\kappa z}, \tag{1}$$

where u_τ is the skin friction velocity and κ is the von Karman constant. The famous log law of the wall follows directly by integration.

However, a recent work by Dallas, Vassilicos and Hewitt [2] advances the idea that this *something* should in fact be the eddy turnover time $\tau \equiv E/\epsilon$, where E is the average kinetic energy per unit mass of the turbulent velocity fluctuations and ϵ is the dissipation rate of

*Corresponding author. Email: j.c.vassilicos@imperial.ac.uk

ISSN: 1468-5248 online only

DOI: 10.1080/146852408.2010.510842
http://www.informaworld.com

this average kinetic energy per unit mass. In this case, the immediate consequence of the intermediate asymptotic assumption is that in the intermediate range $\delta_\nu \ll z \ll h/2$,

$$\tau \approx \frac{3}{2}\kappa_s \frac{z}{u_\tau} \tag{2}$$

in terms of the constant of proportionality $\frac{3}{2}\kappa_s$, where κ_s is the stagnation point von Karman coefficient.

Dallas et al. [2] combined this reformulated intermediate asymptotic assumption with (i) a local balance between energy production and dissipation [3] and with (ii) the fact that, in turbulent channel flows, the energy production takes the asymptotic form $u_\tau^2 \frac{d}{dz}U$ in the limit $h/\delta_\nu \to \infty$ and in the intermediate range $\delta_\nu \ll z \ll h/2$ as a result of the z-integrated momentum balance in the direction of the mean flow. They were therefore led to the conclusion that in this intermediate range,

$$\frac{d}{dz}U \approx \frac{u_\tau}{\kappa_s z}(2E_+/3), \tag{3}$$

where $E_+ \equiv E/u_\tau^2$. If the normalised averaged kinetic energy per unit mass E_+ has no z and/or Reynolds number dependencies in the present intermediate asymptotic range, then their conclusion is the same as the usual one, i.e. Equation (1). However, if E_+ does have such dependencies, then Equation (3) does not imply to Equation (1). Using the high Reynolds number turbulent channel flow data, which Hoyas and Jiménez [5] obtained by Direct Numerical Simulations (DNS), Dallas et al [2] found better support for Equation (3) than for Equation (1), with $E_+ \sim z_+^{-2/15}$ in the intermediate range ($z_+ \equiv z/\delta_\nu$). (Townsend [4] introduced the concept of inactive motions to account for dependencies of E_+ on z and/or a Reynolds number.)

Dallas et al [2] went on to argue that $\tau \approx \frac{3}{2}\kappa_s \frac{z}{u_\tau}$ implies a particular distribution in space of the instantaneous stagnation points of the turbulent fluctuating velocity $\boldsymbol{u}' \equiv \boldsymbol{u} - \langle \boldsymbol{u} \rangle$, where $\langle \boldsymbol{u} \rangle$ is the mean value of the fluid velocity $\boldsymbol{u}$ at a given distance from the channel walls. Specifically, they argued that $\tau \approx \frac{3}{2}\kappa_s \frac{z}{u_\tau}$ implies a number density n_s of such stagnation points which is inversely proportional to z_+ in the intermediate range $\delta_\nu \ll z \lesssim h/2$, i.e.

$$n_s \approx \frac{C_s}{\delta_\nu^3} z_+^{-1}, \tag{4}$$

where $C_s \propto 1/\kappa_s$. They found good supporting DNS evidence for this inverse power-law relation in the range $\delta_\nu \ll z \lesssim h/2$. The spatial distribution of stagnation points with respect to the wall underpins the mean flow profile because Equation (2) leads to Equation (3) and Equation (2) is a reflection of (4).

The stagnation points are objectively and unambiguously well-defined quantities which are bound to be related to coherent structures. Numerous types of coherent structures have been proposed to explain experimentally the observed phenomena in turbulent shear flow. However, the study of the nature and dynamical influence of coherent structures, as well as their own evolutionary dynamics, remains an open research question. Much of this difficulty comes in the myriad of structures, which can be defined, though not without ambiguities (horseshoe- and hairpin-eddies, pancake- and surfboard-eddies, typical eddies, vortex rings, mushroom- and arrowhead-eddies etc.) [6]. In this context, the relation between the spatial distribution of velocity stagnation points and the mean flow profile is valuable.

A motivation to study the motions of these stagnation points follows immediately from their unambiguous definition and relations to coherent structures and their importance in underpinning the mean flow profile. These stagnation points are of course not static and their motions therefore reflect coherent flow structure dynamics behind mean flow profiles. The definition of the velocity $\boldsymbol{V}_s$ of stagnation points (as opposed to the fluid velocity at stagnation points) was introduced by Goto, Osborne, Vassilicos and Haigh [7]:

$$\frac{\partial}{\partial t}\boldsymbol{u}' + \boldsymbol{V}_s \cdot \nabla \boldsymbol{u}' = 0, \tag{5}$$

where $\boldsymbol{u}' = 0$. Hence, the fluid acceleration $\boldsymbol{a} \equiv \frac{\partial}{\partial t}\boldsymbol{u}' + \boldsymbol{u}' \cdot \nabla \boldsymbol{u}'$ controls the motions of stagnation points and, specfically

$$\boldsymbol{a} = -\boldsymbol{V}_s \cdot \nabla \boldsymbol{u}' \tag{6}$$

at stagnation points. As a result, the motions of stagnation points offer in turn an immediate motivation for the study of acceleration statistics in a turbulent channel flow.

Of course, motivations to study acceleration statistics are wider and abound. The acceleration of a fluid element is perhaps the most direct and basic representation of fluid motion, reflecting the resultant of all forces acting on the fluid. As a result acceleration is of great interest for a variety of reasons, ranging from studies of fine scale intermittency [8] to applications in Lagrangian modelling of turbulence and turbulent dispersion [9, 10].

As the material derivative of the velocity vector $\boldsymbol{u}$, the acceleration appears on the left-hand side of the incompressible Navier–Stokes equations

$$\boldsymbol{A} \equiv \frac{D\boldsymbol{u}}{Dt} = \frac{\partial \boldsymbol{u}}{\partial t} + \boldsymbol{u} \cdot \nabla \boldsymbol{u} = \frac{-1}{\rho}\nabla p + \nu \nabla^2 \boldsymbol{u}, \tag{7}$$

where p is the pressure and ρ is the fluid density. Previous acceleration studies have focused on homogeneous isotropic turbulence (HIT). The first studies of acceleration were performed using DNS of HIT [11] and were continued by Vedula and Yeung [8], Yeung [12] and Tsinober, Vedula, and Yeung [13]. On the experimental side it has only been recently possible to perform direct Lagrangian measurements of acceleration by particle tracking [14–16]. Many of these studies have been concerned with the scaling of the acceleration. For instance, La Porta [14] observed Kolmogorov scaling at high Reynolds numbers. On the other hand, Hill [17] has developed a detailed and careful analysis that gives the scaling of acceleration variance at any Reynolds number and argues that Kolmogorov scaling cannot be observed at any Reynolds number. More recently Gulitski et al. [18] have reported hot wire measurements of acceleration from field experiments at Taylor–Reynolds numbers, Re_λ, up to 10^4 and do not find Kolmogorov scaling of the acceleration variance.

This scaling issue depends very sensitively on the so-called random Taylor or sweeping decorrelation hypothesis, first proposed by Tennekes [19], which states that in high Reynolds number turbulence the dissipative eddies flow past an Eulerian observer in a time which is much smaller than the characteristic timescale associated with their dynamics and is determined by the sweeping of small eddies by large ones. Tsinober et al. [13] explain how this hypothesis means that the local and convective accelerations, $\boldsymbol{A}_l \equiv \frac{\partial \boldsymbol{u}}{\partial t}$ and $\boldsymbol{A}_c \equiv \boldsymbol{u} \cdot \nabla \boldsymbol{u}$, tend to anti-align as Reynolds number increases and thereby cancel much of each other so that $\boldsymbol{A} = \boldsymbol{A}_l + \boldsymbol{A}_c$ is much smaller and scales in a very different way than both $\boldsymbol{A}_l$

and $\boldsymbol{A}_c$. Tsinober et al. [13] found compelling DNS evidence that the sweeping decorrelation hypothesis is increasingly observed with increasing Reynolds numbers in HIT. Goto et al. [7] explained how the scaling of the stagnation point velocity $\boldsymbol{V}_s$ is, in fact, the reflection of this sweeping decorrelation hypothesis.

The motivations to study acceleration statistics are all clearly closely interrelated: stagnation points of the fluctuating velocity field partly control the mean flow profile of turbulent channel flows. These result from small-scale turbulence dynamics, which are, at least partly, reflected in the motions of these stagnation points. These are controlled by the acceleration and the velocity fluctuation gradient fields. The scalings of the acceleration and the velocity fluctuation gradient fields with Reynolds number and distance from the wall differ because of the sweeping of small dissipative eddies by large energy containing ones. This sweeping controls the scalings of the acceleration and of the stagnation point velocity $\boldsymbol{V}_s$. However, acceleration studies in wall-bounded turbulence remain very scarce. For a start, $\boldsymbol{A}$ and $\boldsymbol{a}$ differ in such flows, whereas they are the same in HIT, where $\langle \boldsymbol{u} \rangle = 0$.

To the authors' knowledge the only investigation of acceleration in wall-bounded turbulence is that of Christensen and Adrian [20]. They used temporally resolved particle-image velocimetry measurements to determine the acceleration in a turbulent channel flow at friction Reynolds numbers $Re_\tau = 550$ and 1747. They found that the temporal derivative of the velocity in a frame moving with the bulk velocity $\boldsymbol{U}_b$ to be an order of magnitude smaller than the temporal derivative of the velocity in a frame not moving with respect to the wall. Although this gives an initial indication of the nature of sweeping in turbulent channel flow, a more thorough investigation is needed.

This paper aims to give a description of the nature of acceleration in a turbulent channel flow. The layout of the paper is as follows. In Section 2 details of the DNS and of some of our numerical procedures are given before results are presented. In Section 3 we briefly confirm and discuss known mean velocity and vorticity profiles, as well as equation (4) and its relation to the multiscale topography of the flow. Acceleration field decompositions and some of their basic properties are introduced in Section 4 so that Sections 5 and 6 can follow with new results on various mean profiles of the various acceleration fields introduced in Section 4. In Section 7 we confirm Equation (4), discuss its relation to the multi-scale topography of the flow and present statistics and profiles of the stagnation point velocities $\boldsymbol{V}_s$. We conclude in Section 8.

2. Governing equations and summary of numerical method

The governing equations of incompressible turbulent flow, the continuity and the momentum equation, are non-dimensionalised with the channel half height h and the friction velocity u_τ. A schematic of the notation for the channel geometry is given in Figure 1: the mean flow is in the x-direction and the channel walls are normal to the z-axis.

The non-dimensional continuity and rotational form of the momentum equation can then be written (using Einstein summation notation) as

$$\frac{\partial u_j}{\partial x_j} = 0, \tag{8}$$

$$\frac{\partial u_i}{\partial t} = \epsilon_{ijk} u_j \omega_k + \delta_{1i} \Lambda - \frac{\partial \Pi}{\partial x_i} + \frac{1}{Re_\tau} \frac{\partial^2 u_i}{\partial x_j \partial x_j}. \tag{9}$$

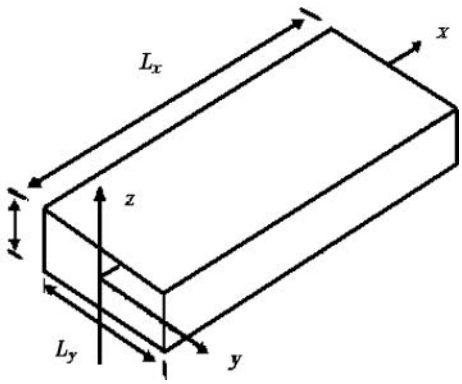

Figure 1. Sketch showing the geometry of the channel flow. Coordinates/velocities are x/u in the streamwise direction, y/v in the spanwise direction and z/w in the wall-normal direction.

Here ω_i is the ith vorticity component, $\omega_i = \epsilon_{ijk}\frac{\partial u_k}{\partial x_j}$, with ϵ_{ijk} being the permutation tensor; $Re_\tau = \frac{u_\tau h}{\nu}$ is the friction Reynolds number; $\Pi = p + u_i u_i/2$ is the modified non-dimensional pressure and $\delta_{1i}\Lambda$ is the driving mean pressure gradient.

Numerical solutions of the above equations are obtained as in [21] using the spectral method of [22], with Fourier methods used for spatial discretisation in the streamwise and transverse directions and Chebyshev methods used in the wall-normal direction. The pressure and viscous terms are treated implicitly to avoid extremely small time steps in the near-wall region. A third-order Runge–Kutta scheme is used to integrate the convective terms. The '3/2 rule' is used for de-aliasing whenever nonlinear quantities are required, with the additional wavenumbers generated by this process truncated.

This paper is concerned with two simulations in large computational domains at different Reynolds numbers ($Re_\tau = 360$ and 720). Details of the simulation are given in Table 1. All statistics are collected only after the simulation has reached a statistically stationary state.

The Reynolds decompositions of the velocity field, i.e. $\boldsymbol{u} = \langle \boldsymbol{u} \rangle + \boldsymbol{u}'$, where $\langle \boldsymbol{u} \rangle = (U(z), 0, 0)$, are obtained by numerically calculating the mean flow as $\langle \boldsymbol{u}(z_k) \rangle = \frac{1}{N_x N_z}\sum_{i=1}^{N_x}\sum_{j=1}^{N_y} \hat{\boldsymbol{u}}(x_i, y_j, z_k),\quad k = 1, \ldots, N_z$. The acceleration due to the fluctuating velocity was calculated both via $\boldsymbol{a} = \frac{\partial \boldsymbol{u}'}{\partial t} + \boldsymbol{u}' \cdot \nabla \boldsymbol{u}'$ and $\boldsymbol{a} = \boldsymbol{A} - \langle \boldsymbol{u} \rangle \cdot \nabla \boldsymbol{u} - \boldsymbol{u} \cdot \nabla \langle \boldsymbol{u} \rangle$ (see Section 4) using a simple first-order finite difference for time derivatives. Both methods give indistinguishable statistics.

Table 1. Details of the two turbulent channel flow simulations. Re_τ is the friction Reynolds number, N_i is the number of grid points in i direction and L_x, L_y and h are shown in Figure 1.

Case	Re_τ	$N_x \times N_y \times N_z$	L_x	L_y	h
A	360	$256 \times 256 \times 161$	12	6	2
B	720	$512 \times 512 \times 321$	24	12	2

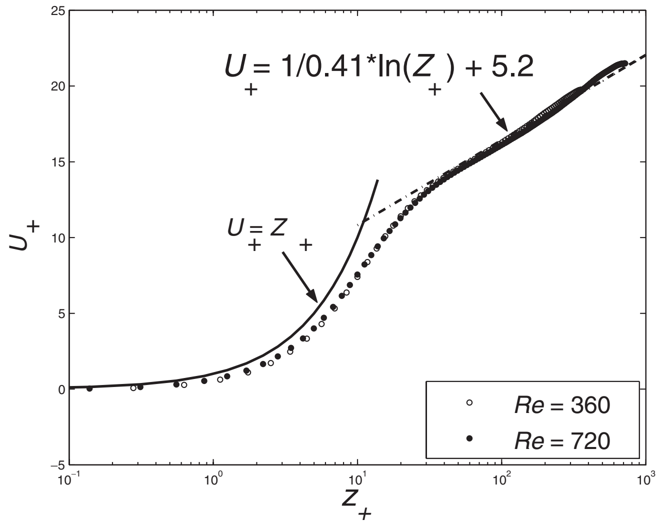

Figure 2. Mean velocity profile for both simulations.

3. Mean velocity and vorticity profiles

As a validation of our numerics, we check some standard statistics of the velocity field as first presented in the seminal paper [23]. The mean velocity is shown in Figure 2, where the wall-normal coordinate is given in wall units $z_+ = z/\delta_\nu$ with $\delta_\nu = \nu/u_\tau$. The velocity is normalised by the friction velocity, $U_+ = U/u_\tau$, with $U = \langle u \rangle$ and $\langle \ldots \rangle$ denoting spatial averaging. Our data show the usual DNS agreement with $U_+ = z_+$ at very small values of z_+. Furthermore, $U_+ = \frac{1}{0.41} \log z_+ + 5.2$ provides an approximate fit of the data in a candidate intermediate z_+ region above 30 and well below Re_τ, as is also usual with such DNS data.

The root mean square (rms) values of velocity component fluctuations, u_{rms}, are shown in Figure 3. Antonia and Kim [24] indicated that the Reynolds number effect on the turbulent intensity in the spanwise direction is significantly larger than in the other two directions. In the present study both spanwise and wall-normal rms velocity fluctuations increase with Reynolds number. However, the rms value of the streamwise velocity fluctuations shows negligible change as we increase the Reynolds number, which is not consistent with [25]. We believe, this difference results from the lower accuracy of the finite difference method compared to the spectral method employed here. It is also worth noting that the peak values of u_{rms} in the spanwise and wall-normal directions move away from the wall in terms of wall units as Re_τ increases, whereas the peak value of the streamwise u_{rms} does not.

The rms of vorticity normalised by wall variables, i.e. $(\omega_+)_{\mathrm{rms}} = \frac{\omega_{\mathrm{rms}}\delta_\nu}{u_\tau}$ is shown in Figure 4. The differences between the two Reynolds numbers are insignificant except in the near-wall region, where the rms value of the vorticity increases with increasing Reynolds number. Note, in passing, how the flow is clearly not two-dimensional near the walls. At values of z_+ larger than about 30, all three vorticity curves more or less collapse on each other, thus providing evidence of small-scale isotropy far enough away from the walls. Our results are in qualitative agreement with those of [25], who studied turbulent channel flows at $Re_\tau = 160, 395$ and 640.

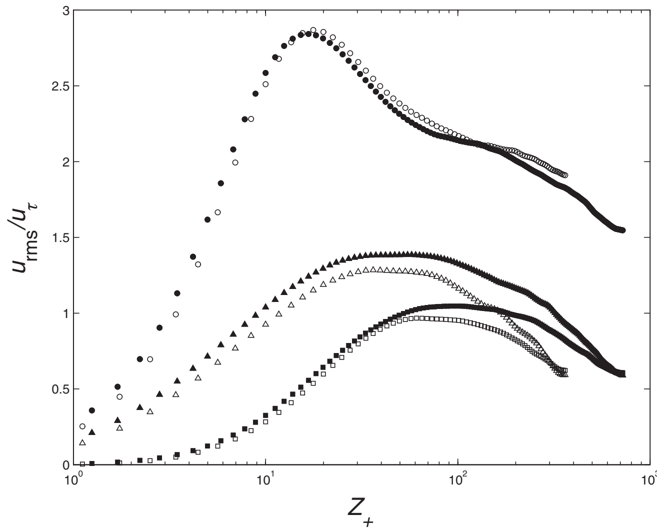

Figure 3. Root mean square value of turbulence intensity. Circles indicate streamwise, triangles spanwise and squares wall-normal. Open and filled symbols are for $Re_\tau = 360$ and 720, respectively.

4. Acceleration field of turbulent channel flow

In the introduction we alluded to the fact that $\boldsymbol{A} \equiv \frac{\partial \boldsymbol{u}}{\partial t} + \boldsymbol{u} \cdot \nabla \boldsymbol{u}$ and $\boldsymbol{a} \equiv \frac{\partial \boldsymbol{u}'}{\partial t} + \boldsymbol{u}' \cdot \nabla \boldsymbol{u}'$ are different in turbulent channel flows even though they are equal in HIT, where $\langle \boldsymbol{u} \rangle = 0$. In a statistically stationary turbulent channel flow where $\langle \boldsymbol{u} \rangle = (U(z), 0, 0)$ and $\frac{\partial \langle \boldsymbol{u} \rangle}{\partial t} + \langle \boldsymbol{u} \rangle \cdot$

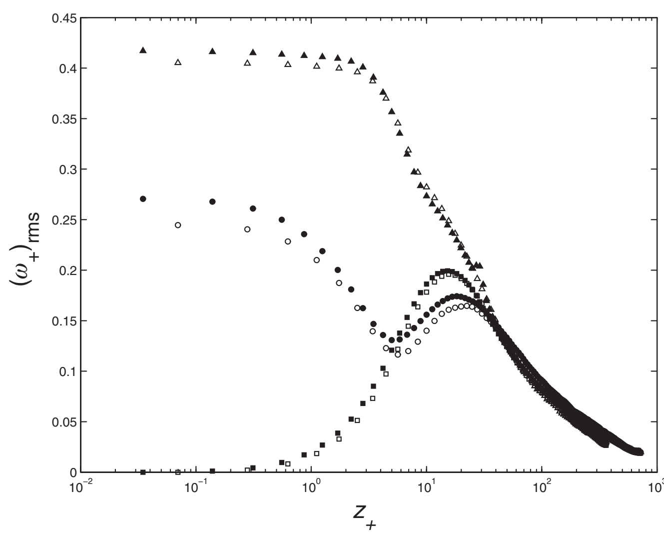

Figure 4. Root mean square value of vorticity normalised by wall variables. Circles indicate vorticity in the streamwise, triangles in the spanwise and squares in the wall-normal directions. Open and filled symbols are for $Re_\tau = 360$ and 720, respectively.

$\nabla\langle \boldsymbol{u}\rangle = \boldsymbol{0}$,

$$\boldsymbol{A} = \boldsymbol{a} + \langle \boldsymbol{u}\rangle \cdot \nabla \boldsymbol{u}' + \boldsymbol{u}' \cdot \nabla\langle \boldsymbol{u}\rangle. \tag{10}$$

This decomposition of the acceleration field has the property

$$\langle \boldsymbol{A}\rangle = \langle \boldsymbol{a}\rangle \tag{11}$$

$$= -\frac{1}{\rho}\nabla\langle p\rangle + \nu\nabla^2\langle \boldsymbol{u}\rangle. \tag{12}$$

Furthermore, incompressibility and statistical stationarity imply that the first moments of the acceleration components give the Reynolds stress gradients, i.e.

$$\langle a_i\rangle = \frac{\partial}{\partial x_j}\langle u_j' u_i'\rangle. \tag{13}$$

Following [28] we also decompose each acceleration field $\boldsymbol{A}$ and $\boldsymbol{a}$ into local and convective accelerations, i.e. $\boldsymbol{A} = \boldsymbol{A}_l + \boldsymbol{A}_c$, where $\boldsymbol{A}_l = \frac{\partial \boldsymbol{u}}{\partial t}$ and $\boldsymbol{A}_c = \boldsymbol{u} \cdot \nabla \boldsymbol{u}$, and $\boldsymbol{a} = \boldsymbol{a}_l + \boldsymbol{a}_c$, where $\boldsymbol{a}_l = \frac{\partial \boldsymbol{u}'}{\partial t}$ and $\boldsymbol{a}_c = \boldsymbol{u}' \cdot \nabla \boldsymbol{u}'$. Note that of all these acceleration terms, only the total acceleration $\boldsymbol{A}$ and the convective 'fully fluctuating' acceleration $\boldsymbol{a}_c$ are Galilean invariant. The Eulerian constituents $\boldsymbol{A}_l$ and $\boldsymbol{A}_c$ of the Lagrangian total $\boldsymbol{A}$ are not Galilean invariant, and neither are $\boldsymbol{a}$ and $\boldsymbol{a}_l$.

Also note that $\langle \boldsymbol{A}_l\rangle = \langle \boldsymbol{a}_l\rangle = 0$ and that

$$\langle \boldsymbol{A}\rangle = \langle \boldsymbol{A}_c\rangle = \langle \boldsymbol{a}\rangle = \langle \boldsymbol{a}_c\rangle. \tag{14}$$

5. Mean acceleration profiles in turbulent channel flow

In this section we calculate the three average acceleration profiles $\langle A_x\rangle = \langle a_x\rangle$, $\langle A_y\rangle = \langle a_y\rangle$ and $\langle A_z\rangle = \langle a_z\rangle$ (as functions of z).

As explained in [1], assuming the turbulence to be statistically stationary and effectively homogeneous in all directions except z, the wall-normal mean momentum equation implies

$$\frac{\partial\langle p\rangle}{\partial x} = \frac{dp_w}{dx}, \tag{15}$$

where $p_w = \langle p(x, 0, 0)\rangle$ is the mean pressure on the bottom wall. From the streamwise mean momentum equation one obtains

$$\frac{d\tau}{dz} = \frac{dp_w}{dx}, \tag{16}$$

where the total shear stress $\tau(z)$ is given by

$$\tau = \rho\nu\frac{dU}{dz} - \rho\langle uw\rangle. \tag{17}$$

In the near-wall region, for fixed time and space, the normalised fluctuating velocity components $u_+ \equiv u/u_\tau$, $v_+ \equiv v/u_\tau$ and $w_+ \equiv w/u_\tau$ can be written as Taylor series expansions as in [1],

$$u_+ = b_1 z_+ + c_1 z_+^2 + \dots, \tag{18}$$

$$v_+ = b_2 z_+ + c_2 z_+^2 + \dots, \tag{19}$$

$$w_+ = c_3 z_+^2 + \dots, \tag{20}$$

where the boundary conditions $u = v = w = 0$ and $\omega_z = 0$ at the wall have all been taken into account. The mean streamwise acceleration $\langle a_x \rangle = \frac{\partial}{\partial z}\langle uw \rangle$ and in the viscous sublayer $z_+ < 5$, it then follows that

$$\langle a_x \rangle = \frac{\partial}{\partial z}\langle uw \rangle \tag{21}$$

$$= -3\sigma \frac{u_\tau^2}{\delta_\nu} z_+^2, \tag{22}$$

where the non-dimensional coefficient $\sigma = b_1 c_3$ may be assumed to be independent of Reynolds number.

In the intermediate layer, $30 < z_+$ and $z/h < 0.3$, if we assume a log law (1) for simplicity, i.e. $\frac{\partial^2 U_+}{\partial z_+^2} = -\frac{1}{\kappa} z_+^{-2}$, and do not take into account a possible correction resulting from a z-dependent E_+ on Equation (3), then

$$\langle a_x \rangle = \frac{\partial}{\partial z}\langle uw \rangle \tag{23}$$

$$= \frac{2u_\tau^2}{h} - \nu \frac{u_\tau}{\delta_\nu^2 \kappa} z_+^{-2} \tag{24}$$

$$= \frac{u_\tau^2}{\delta_\nu}\left(2\frac{\delta_\nu}{h} - \frac{1}{\kappa} z_+^{-2}\right), \tag{25}$$

where use has been made of the fact that $-\frac{1}{\rho}\frac{\partial <p>}{\partial x} = \frac{2u_\tau^2}{h}$. This implies, in particular, that as z_+ increases towards the centre of the channel, $\langle a_x \rangle \to \frac{2u_\tau^2}{h} \neq 0$. These estimates are in sufficiently good agreement with our simulations as shown in Figures 5 and 6(a).

In the spanwise direction, we have

$$v\left(\frac{\partial u}{\partial x} + \frac{\partial v}{\partial y} + \frac{\partial w}{\partial z}\right) = 0 \tag{26}$$

from the incompressibility condition. Substituting Equation 26 into the definition $A_y = \frac{\partial v}{\partial t} + u\frac{\partial v}{\partial x} + v\frac{\partial v}{\partial y} + w\frac{\partial v}{\partial z}$, and averaging with the assumptions of statistical stationarity and homogeneity in the streamwise and spanwise directions, leads to

$$\langle A_y \rangle = \langle a_y \rangle = 0. \tag{27}$$

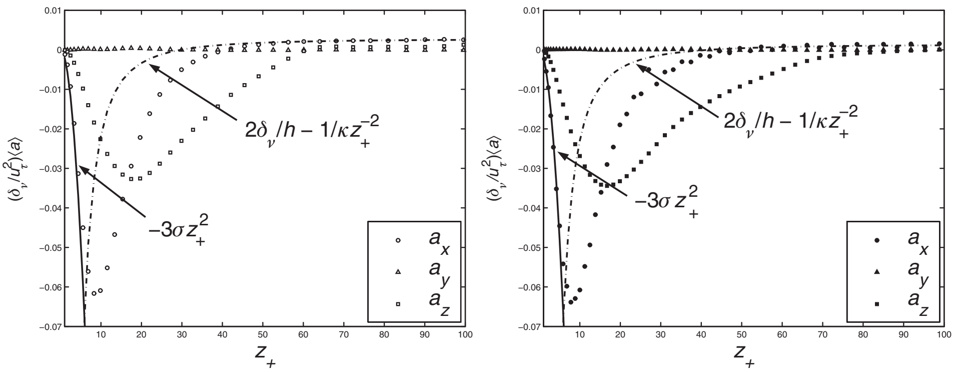

(a) $Re_\tau = 360$. (b) $Re_\tau = 720$.

Figure 5. Average acceleration profiles for all three acceleration components as indicated by the legend.

Similar analysis in the wall-normal direction under the same assumptions gives

$$\langle A_z \rangle = \langle a_z \rangle = \frac{\partial \langle w^2 \rangle}{\partial z}. \tag{28}$$

This conclusion is also confirmed by our data as shown in Figures 5 and 6(b). The Reynolds number dependencies appear insignificant in this data. The minimum value of the averaged streamwise acceleration appears at $z_+ = 9$ for both Reynolds numbers, while the minimum value of the averaged acceleration in the wall-normal direction is at $z_+ = 18$.

6. Quadratic mean acceleration profiles in turbulent channel flow

The Reynolds number scaling of the acceleration variance mentioned in the Introduction was first studied by Heisenberg [29] and Yaglom [30] in the HIT case. By direct application of Kolmogorov scaling they obtained $\langle a_i a_j \rangle = a_0 \epsilon^{3/2} \nu^{-1/2} \delta_{ij}$, where a_0 is a universal constant

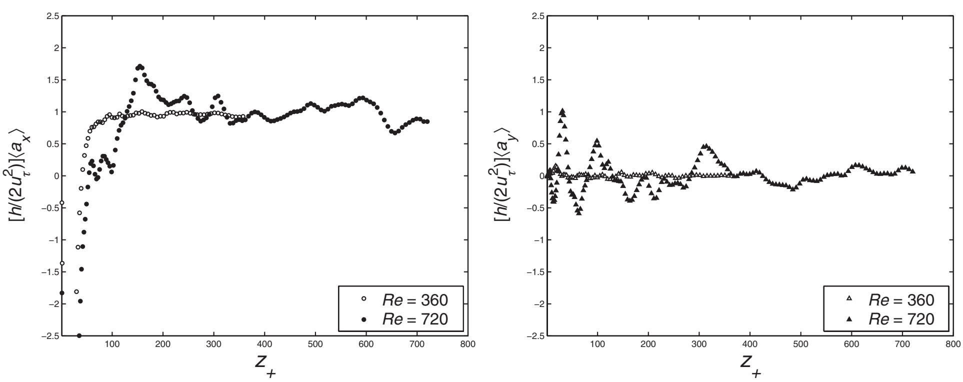

(a) (b)

Figure 6. Mean acceleration normalised by $2u_\tau^2/h$ in all three directions for $Re_\tau = 360$ and 720. (a) shows the streamwise and (b) the spanwise directions.

independent of Reynolds number and ϵ is the kinetic energy dissipation per unit mass. It is only relatively recently that it has become possible to measure acceleration statistics in the laboratory, and the evidence resulting from these measurements as well as DNS and theoretical results are not in clear agreement with each other and are shedding doubt on the universality of a_0, including its presumed Reynolds number independence (see references mentioned in the Introduction).

In wall-bounded turbulence, the Reynolds number and the dissipation rate are effectively functions of distance to the wall so that arguments such as those of [29] and [30] lead to z-dependencies of acceleration variances. Also, there are more acceleration terms which are of interest in wall-bounded turbulence than in HIT. In turbulent channel flows we need to consider the variances of $\boldsymbol{A}$ and $\boldsymbol{a}$ and of the terms by which they differ, i.e. $\langle \boldsymbol{u} \rangle \cdot \nabla \boldsymbol{u}'$ and $\boldsymbol{u}' \cdot \nabla \langle \boldsymbol{u} \rangle$.

6.1. *Quadratic mean profiles of* $\langle \boldsymbol{u} \rangle \cdot \nabla \boldsymbol{u}'$ *and* $\boldsymbol{u}' \cdot \nabla \langle \boldsymbol{u} \rangle$

We start with z-profiles of the variances of $\langle \boldsymbol{u} \rangle \cdot \nabla \boldsymbol{u}'$ and $\boldsymbol{u}' \cdot \nabla \langle \boldsymbol{u} \rangle$ in the intermediate layer where we may assume classical log-layer and Kolmogorov scalings to be good starting approximations. We therefore scale $\langle \boldsymbol{u} \rangle = (U, 0, 0)$ with u_τ, gradients of U with u_τ/z and gradients of turbulent velocity fluctuations $\boldsymbol{u}'$ with u_η/η, where η is the Kolmogorov lengthscale at distance z from the wall and u_η is the Kolmolgorov velocity at that distance. Note, however, that turbulent velocity fluctuations themselves are assumed to scale with u_τ.

Firstly we consider the term $\boldsymbol{u}' \cdot \nabla U$. Figure 7 shows that the rms of this term exhibits a clear power law dependence on z_+ with exponent -1 for $z_+ > 30$ and $z/h < 0.3$, i.e. the range where our DNS shows approximate agreement with the log law in Figure 2. This is a

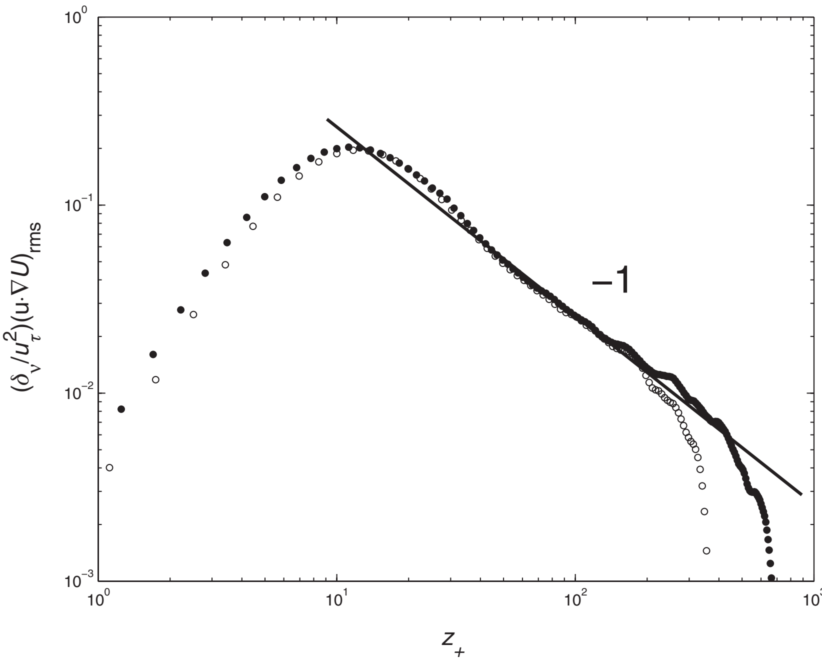

Figure 7. Rms value of $\boldsymbol{u}' \cdot \nabla U$. Open symbols indicate $Re_\tau = 360$ and filled symbols $Re_\tau = 720$.

range which increases with Reynolds number and this -1 power law can be seen as resulting directly from classical log-layer scalings, i.e. $\boldsymbol{u}' \cdot \nabla U \sim u_\tau u_\tau / z$.

Secondly, we consider the term $\langle \boldsymbol{u} \rangle \cdot \nabla \boldsymbol{u}' = U \frac{\partial}{\partial x} \boldsymbol{u}'$. On the basis of classical log-law and Kolmogorov scalings, the rms of this term can be estimated as follows in the intermediate log-layer-like region:

$$\langle \boldsymbol{u} \rangle \cdot \nabla \boldsymbol{u}' \sim U \frac{u_\eta}{\eta} \tag{29}$$

$$\sim u_\tau \left(\frac{\log z_+}{0.41} + 5.2 \right) \frac{(\epsilon \eta)^{1/3}}{\eta} \tag{30}$$

$$\sim \left(\frac{\log z_+}{0.41} + 5.2 \right) \frac{u_\tau^2}{\delta_\nu} z_+^{-1/2}, \tag{31}$$

where we have made use of $\epsilon \sim u_\tau^3 / z$, which is the classical expectation in the log-layer [1], and of $\eta \sim (\nu^3/\epsilon)^{1/4}$ and $\delta_\nu = \nu / u_\tau$. Figure 8 shows the z_+-profile of the rms of $\langle \boldsymbol{u} \rangle \cdot \nabla \boldsymbol{u}'$ for all three components of $\boldsymbol{u}'$ and for both Reynolds numbers. These rms profiles do not show clear agreement with our estimate in Equation (31) except, perhaps, for the streamwise component when plotted as $(\boldsymbol{U} \cdot \nabla u)/(\log z_+/\kappa + c)$ versus z_+ (see Figure 8(b)). However, it is clear that all the variances of each component of $\langle \boldsymbol{u} \rangle \cdot \nabla \boldsymbol{u}' = U \frac{\partial}{\partial x} \boldsymbol{u}'$ increase when moving away from the wall, reach a peak and then decrease when moving towards the centre of the channel as qualitatively predicted by Equation (31). The peak value in the streamwise direction is at $z_+ = 30$ and the peak values in the spanwise and wall-normal directions are at $z_+ = 70$.

6.2. *Quadratic mean profiles of A*

The total acceleration $\boldsymbol{A}$ can be decomposed as a sum of the local acceleration $\boldsymbol{A}_l = \partial \boldsymbol{u} / \partial t$, which expresses the rate of change of velocity $\boldsymbol{u}$ due to unsteadiness at a fixed point in

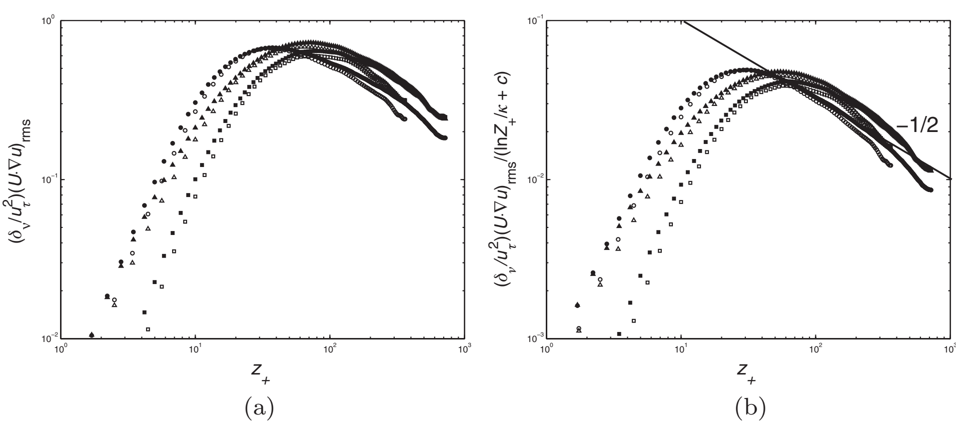

Figure 8. Rms value of $\langle \boldsymbol{u} \rangle \cdot \nabla \boldsymbol{u}'$ (a) normalised by u_τ^2/δ_ν and (b) normalised by $\frac{u_\tau^2}{\delta_\nu}(\frac{\log z_+}{\kappa} + c)$. Circles indicate u, triangles v and squares w. Open symbols indicate $Re_\tau = 360$ and filled symbols $Re_\tau = 720$.

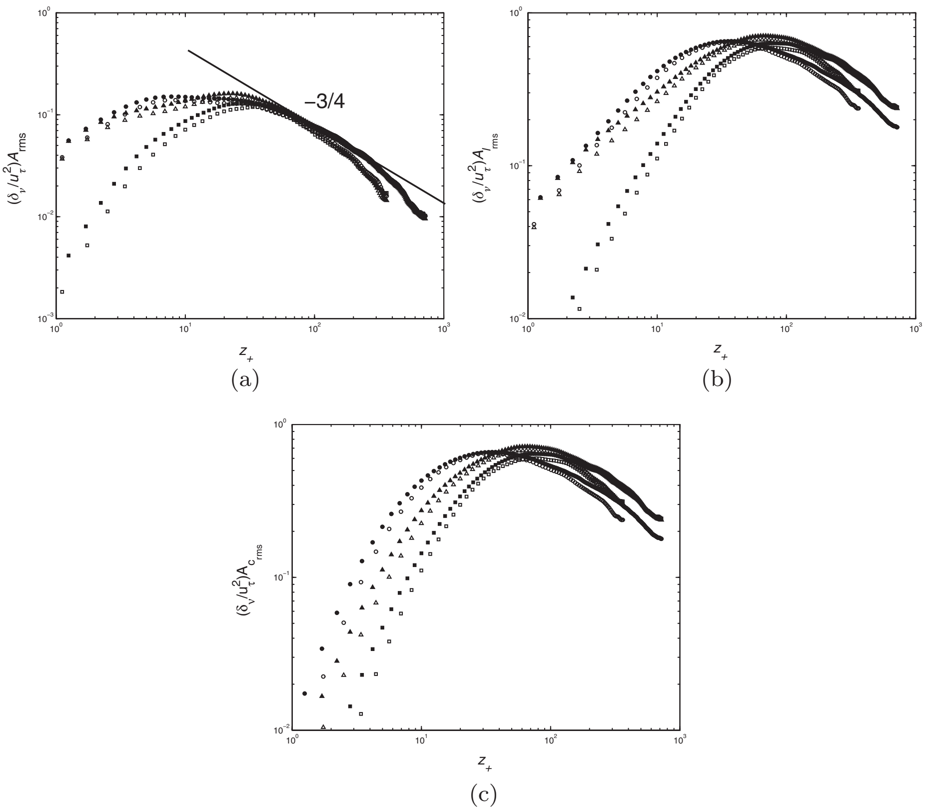

Figure 9. Rms value of acceleration terms. Circles indicate streamwise, triangles spanwise and squares wall-normal. Open and filled symbols are for $Re_\tau = 360$ and 720, respectively. (a) Total acceleration A_{rms}, (b) local acceleration $A_{l,\mathrm{rms}}$ and (c) convective acceleration $A_{c,\mathrm{rms}}$.

space, and the convective acceleration $\boldsymbol{A}_c = \boldsymbol{u} \cdot \nabla \boldsymbol{u}$, which expresses the rate of change of velocity $\boldsymbol{u}$ due to convection past a fixed point in space.

Figure 9 shows the rms values of these total, local and convective accelerations. The rms values normalised by u_τ^2/δ_ν increase slightly with increasing Reynolds number. In the case of the higher Reynolds number $Re_\tau = 720$, the total acceleration $\boldsymbol{A}$ seems to be showing a power law scaling with distance from the wall in the intermediate log-like layer. The exponent of this power law is $-3/4$. This scaling can in fact be obtained from a Kolmogorov estimate of the rms of $\boldsymbol{A}$ as follows:

$$\boldsymbol{A} = \frac{D\boldsymbol{u}}{Dt} \tag{32}$$

$$\sim \frac{u_\eta^2}{\eta} \tag{33}$$

$$\sim \frac{\left(u_\tau z_+^{-1/4}\right)^2}{\delta_\nu^{3/4} z_+^{1/4}} \tag{34}$$

$$\sim \frac{u_\tau^2}{\delta_\nu} z_+^{-3/4}. \tag{35}$$

This scaling seems to be confirmed by our simulations only in the case of higher Reynolds number (Figure 9(a)) presumably because of the larger span of the log-like layer. However, the z-profiles of the rms values of the local and convective accelerations have a less clear form. Note that, while the Galilean-invariant Lagrangian acceleration $\boldsymbol{A}$ may indeed be estimated by Kolmogorov scaling as shown above, the non-Galilean-invariant Eulerian accelerations cannot be estimated in this way. Instead, in the frame where the walls of the channel are not moving, one may write (in terms of dimensionless constants α, β and β')

$$\boldsymbol{A}_c = \boldsymbol{u} \cdot \nabla \boldsymbol{u} \tag{36}$$

$$\sim u_\tau \left(\alpha \frac{u_\tau}{z} + \beta \frac{u_\eta}{\eta} \right) \tag{37}$$

$$\sim \frac{u_\tau^2}{\delta_\nu} \left(\alpha z_+^{-1} + \beta' z_+^{-1/2} \right) \tag{38}$$

with a neglected additive correction which has the same form but multiplied by $\log z_+$. A similar estimate can be made for the rms of $\boldsymbol{A}_l$. The dominant scaling term will be $z_+^{-1/2}$ at high enough Reynolds number and z_+, but our present Reynolds numbers are not high enough for this to be visible (see Figure 9(b) and (c) where the rms values of $\boldsymbol{A}_l$ and $\boldsymbol{A}_c$ are plotted). However, one can venture to conclude from the above estimates that the rms of $\boldsymbol{A}_l$ and $\boldsymbol{A}_c$ are larger than the rms of $\boldsymbol{A}$. This conclusion is confirmed by our simulations as shown in Figure 10(a) and (b).

Tsinober et al. [13] showed that in homogeneous isotropic turbulence the local and convective accelerations are approximately of the same magnitude but anti-aligned and thus cancel each other to produce a smaller total acceleration. This is predicted by the random Taylor or sweeping decorrelation hypothesis [19] whereby small eddies in turbulent flow are passively swept by large eddies. Figure 10 shows that something similar is the case in our simulations for the total acceleration $\boldsymbol{A}$ throughout the flow, except near the wall, i.e. $z_+ < 10$, where the fluctuations of the local acceleration $\boldsymbol{A}_l$ are the dominant contributor to the fluctuations of the total acceleration $\boldsymbol{A}$. It is clear from Figures 10(a) and (b) that the variance of the total acceleration $\boldsymbol{A}$ is much smaller than the variances of both $\boldsymbol{A}_l$ and $\boldsymbol{A}_c$ for $z_+ > 10$, while figure 10(c) shows that the variances of $\boldsymbol{A}_l$ and $\boldsymbol{A}_c$ have approximately the same magnitude for $z_+ > 10$. However, from Sections 4 and 5 we know that $\langle \boldsymbol{A}_l \rangle = 0$ whereas $\langle \boldsymbol{A}_c \rangle \neq 0$. Therefore our conclusion is that the local and convective accelerations $\boldsymbol{A}_l$ and $\boldsymbol{A}_c$ are not approximately the same in magnitude and anti-aligned, but that the fluctuations around their mean values are a conclusion which is confirmed by the PDF of the cosine of the angle between $\boldsymbol{A}_c - < \boldsymbol{A}_c >$ and $\boldsymbol{A}_l - < \boldsymbol{A}_l >$ as shown in Figure 10(d). This conclusion is effectively the same as that of [13] except that in HIT the mean values of both the local and convective accelerations are zero. The correct generalisation of the result obtained by [13] for HIT is therefore the statement that it is the fluctuations of the convective and local accelerations around their means that approximately cancel each other and not the convective and local accelerations themselves.

6.3. *Quadratic mean profiles of a*

We now turn our attention to the profiles of the variances of the acceleration $\boldsymbol{a}$ and its constituent components $\boldsymbol{a}_l \equiv \partial \boldsymbol{u}'/\partial t$ and $\boldsymbol{a}_c \equiv \boldsymbol{u}' \cdot \nabla \boldsymbol{u}'$. Of these, only the convective

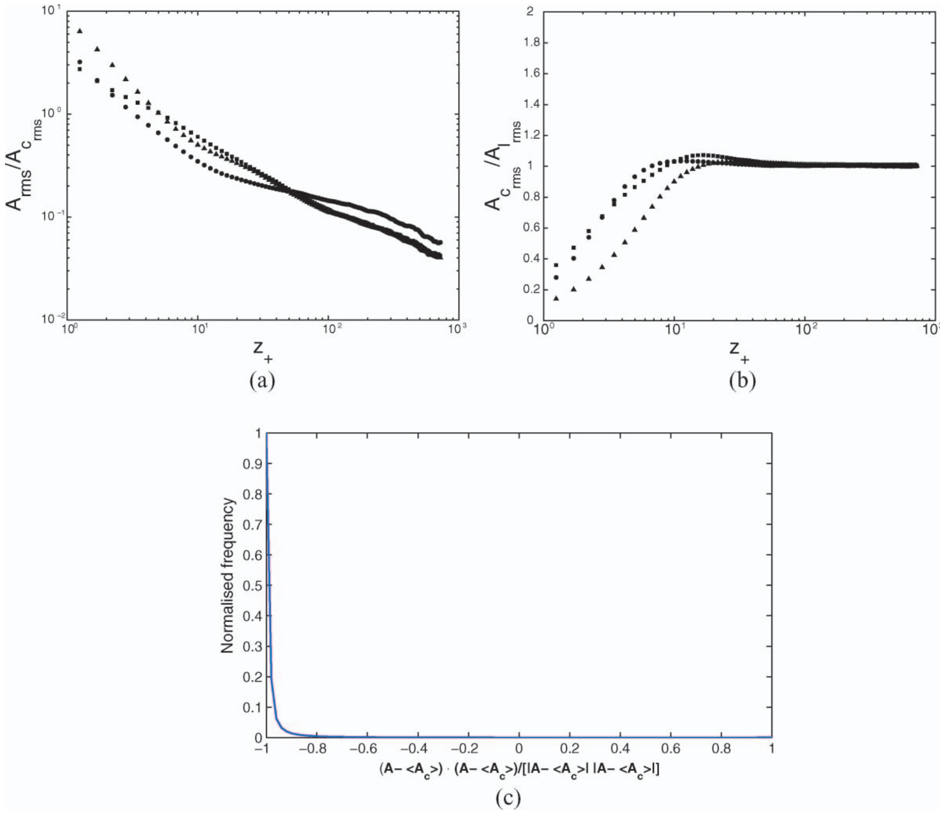

Figure 10. Ratios of rms values of acceleration terms and (d) PDF of the cosine of the angle between $\boldsymbol{A}_c - < \boldsymbol{A}_c >$ and $\boldsymbol{A}_l - < \boldsymbol{A}_l >$ sampled over the region of the channel which is more than 10 wall unit lengths away from both walls. Circles indicate streamwise, triangles spanwise and squares wall-normal. (a) $A_{\mathrm{rms}}/A_{l,\mathrm{rms}}$, (b) $A_{\mathrm{rms}}/A_{c,\mathrm{rms}}$ and (c) $A_{c,\mathrm{rms}}/A_{l,\mathrm{rms}}$. $Re_\tau = 720$.

acceleration $\boldsymbol{a}_c$ is Galilean invariant and so we calculate all quantities in the frame where the walls of the channel are stationary.

On the basis of the conventional type of scaling arguments already used in this work, we may expect the rms of $\boldsymbol{a}_c$ to scale as follows in the intermediate log-like layer:

$$\boldsymbol{a}_c \equiv \boldsymbol{u'} \cdot \nabla \boldsymbol{u'} \sim u_{rms} \frac{u_\eta}{\eta} \tag{39}$$

$$\sim u_\tau \frac{u_\tau z_+^{-1/4}}{\delta_\nu^{3/4} z_+^{1/4}} \tag{40}$$

$$\sim \frac{u_\tau^2}{\delta_\nu} z_+^{-1/2}, \tag{41}$$

where $u_{\rm rms}$ is a characteristic fluctuating velocity rms. Similarly we may expect the rms of $\boldsymbol{a}_l$ to scale as

$$\boldsymbol{a}_l \equiv \frac{\partial \boldsymbol{u}'}{\partial t} \sim U\frac{u_\eta}{\eta} \tag{42}$$

$$\sim u_\tau \frac{u_\tau z_+^{-1/4}}{\delta_\nu^{3/4} z_+^{1/4}} \tag{43}$$

$$\sim \frac{u_\tau^2}{\delta_\nu} z_+^{-1/2} \tag{44}$$

in the intermediate log-like layer.

These scalings are neither clearly consistent nor clearly inconsistent with the results plotted in Figures 11(b) and (c). In particular, Figure 11 shows that the rms values of all three quantities normalised by u_τ^2/δ_ν are larger for our larger Reynolds number at all distances from the wall. This is inconsistent with Equations (41) and (44) but may be due to our relatively low Reynolds numbers, an issue which cannot be resolved in this paper. Also,

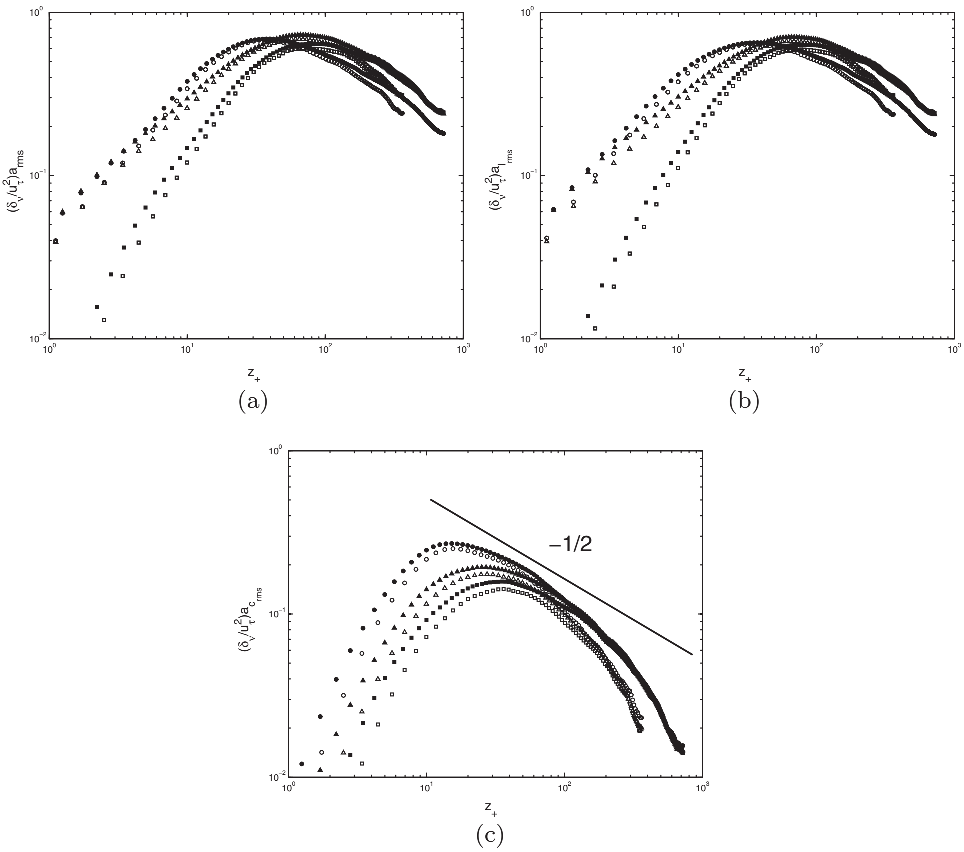

Figure 11. Rms value of terms constituting the acceleration due to the fluctuating velocity. Circles indicate streamwise, triangles spanwise and squares wall-normal. Open and filled symbols are for $Re_\tau = 360$ and 720, respectively. (a) Total acceleration $a_{\rm rms}$, (b) local acceleration $a_{l,\rm rms}$ and (c) convective acceleration $a_{c,\rm rms}$.

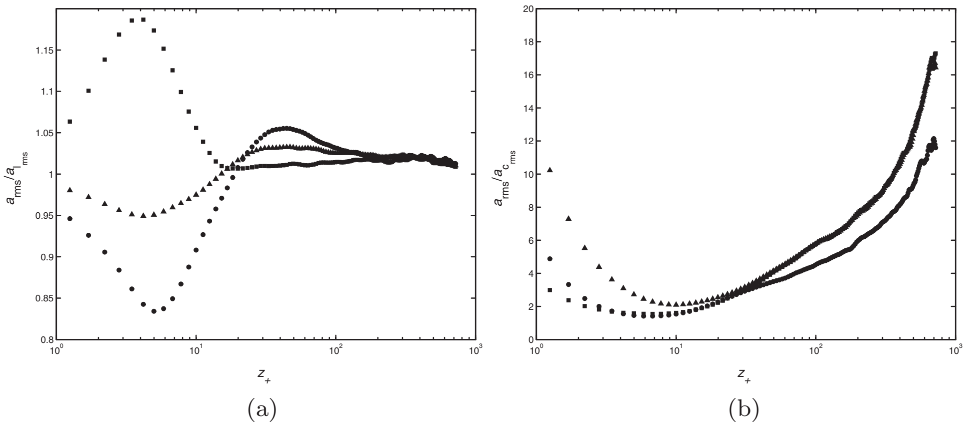

Figure 12. Ratio of rms values of acceleration due to the fluctuating velocity terms. Circles indicate streamwise, triangles spanwise and squares wall-normal. (a) $a_{\rm rms}/a_{l,{\rm rms}}$, (b) $a_{\rm rms}/a_{c,{\rm rms}}$. $Re_\tau = 720$.

there are no clear power-law dependencies on z_+ at distances $z_+ \geq 30$. In fact, if the figures are studied carefully the profiles in all three directions appear different for all three terms and it is unclear at this stage how these differences might change with Reynolds number. The one conclusion, however, which is clear from our results, as can be seen in Figure 11 but much more clearly in Figure 12, is that $|\boldsymbol{a}_c| \ll |\boldsymbol{a}_l| \sim |\boldsymbol{a}|$ in the region where $z_+ \geq 20$. This conclusion is in agreement with Equations (39) and (42) and the fact that $u_{\rm rms} \ll U$.

7. Stagnation point statistics

The statistics of stagnation point velocities $\boldsymbol{V}_s$ follow from those of accelerations $\mathbf{a}$ and fluctuating velocity gradients at stagnation points because of Equation (6). In this section we present some results on the statistics of stagnation points and their velocities $\boldsymbol{V}_s$ in a turbulent channel flow.

We first locate stagnation points $\boldsymbol{u}' = 0$ numerically with a Newton–Raphson method underpinned by a fourth-order Lagrange interpolation. In this we follow the procedure detailed in the Appendix of [2] (the threshold below which we consider a displacement by a Newton–Raphson iteration to be zero is 10^{-5} for single precision – we have chosen this threshold after some experimentation and our results remain the same if the threshold is varied by an order of magnitude. We then count the number N_s of stagnation points within a thin slab of dimension $L_x \times L_y \times \delta_z$, where δ_z is the thickness of the slab. Figure 13 shows how the number of velocity stagnation points increases from the wall and then decreases towards the centre of the channel, taking a peak at $z_+ = 20$. It is clear from Figure 13 that the number density, $n_s = \frac{N_s}{L_x L_y \delta_z}$ of zero-velocity points in a thin slab of dimension $L_x \times L_y \times \delta_z$ (in this figure $\delta_z = \delta_\nu$) parallel to the wall and at a distance z from it, is in agreement with the z_+^{-1} scaling in Equation (4). Note that Equation (4) was established by [2] with a different DNS code.

Before moving to the statistics of $\mathbf{V_s}$, it is worth observing that the decrease of the number of stagnation points with distance from the wall in the region $z_+ \geq 30$ is in qualitative agreement with the increase of streak size with distance from the wall in that same region (see Figure 14) and with the schematic picture of multi-size attached eddies proposed in [26] (see Figure 15). However, it cannot be expected that all stagnation points

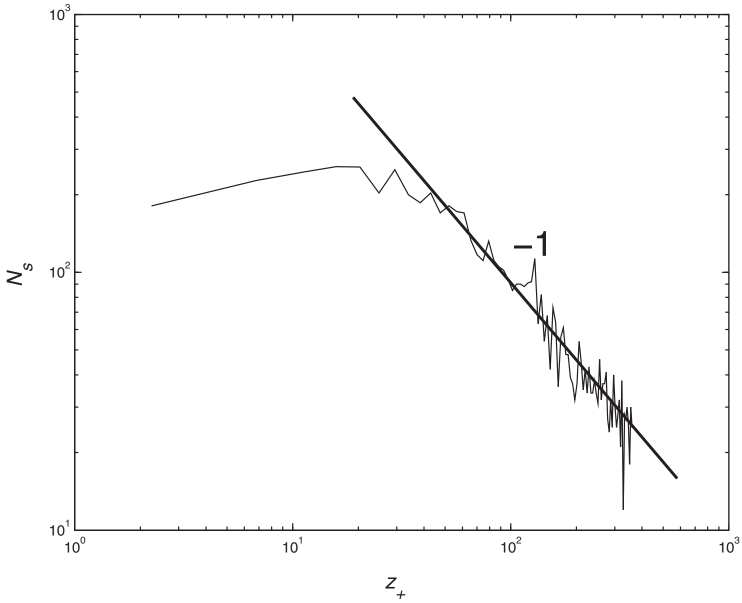

Figure 13. Number of zero-velocity points as a function of distance from the wall for $Re_\tau = 360$.

correspond to attached eddies, as many of them must also result from small wall-free turbulent eddies. Davila and Vassilicos [27] showed that the number density of stagnation points in HIT is proportional to $(L/\eta)^2$, where L is the integral length-scale, $\eta \sim (\nu^3/\epsilon)^{1/4}$ and ϵ is the kinetic energy dissipation rate per unit mass. Assuming local HIT at a distance z from the wall in the region $z_+ \geq 30$, the number N_s of stagnation points within a thin slab of dimension $L_x \times L_y \times \delta_\nu$ can then be estimated as $N_s \approx \frac{L_x L_y \delta_\nu}{L_x^3} C_a(z_+)(L/\eta)^2$, where $L \sim z$, $\eta \sim (\nu^3/\epsilon)^{1/4} \sim \delta_\nu^{3/4} z^{1/4}$ (see [1]) and $C_a(z_+)/L_x^3$ is the number density of attached eddies at a distance z from the wall. Comparing with $N_s \sim \frac{L_x L_y}{\delta_\nu^2} z_+^{-1}$ which results from Equation (4), it follows that $C_a/L_x^3 \sim \delta_\nu^{-3} z_+^{-5/2}$. This would be the scaling for stagnation points related to the attached eddies. It is not the same as the scaling in Equation (4) for all stagnation points.

We now use Equation (6) to calculate $\langle \boldsymbol{V}_s \rangle_{sp}$, where the notation $\langle \ldots \rangle_{sp}$ means an average over the stagnation points which have been found in a thin slice parallel to the channel walls. These slices are of dimension $L_x \times L_y \times \delta_z$, where δ_z is the thickness of the slice. The number of stagnation points in such slices as a function of the slice's distance z from the closest channel wall are given in Figure 13. In Figure 16 we plot the profiles of the three components of $\langle \boldsymbol{V}_s \rangle_{sp}$ as functions of z_+. In calculating these statistics, no component of $\mathbf{V_s}$ was found larger than $150u_\tau$. It is clear that stagnation points do not have a clear mean motion towards the walls or in the spanwise direction. However, they do move on average along the streamwise direction with an average speed which seems to be close to the average fluid velocity at these points, i.e.

$$\langle \boldsymbol{V}_s \rangle_{sp} \approx \langle \boldsymbol{u} \rangle_{sp}. \tag{45}$$

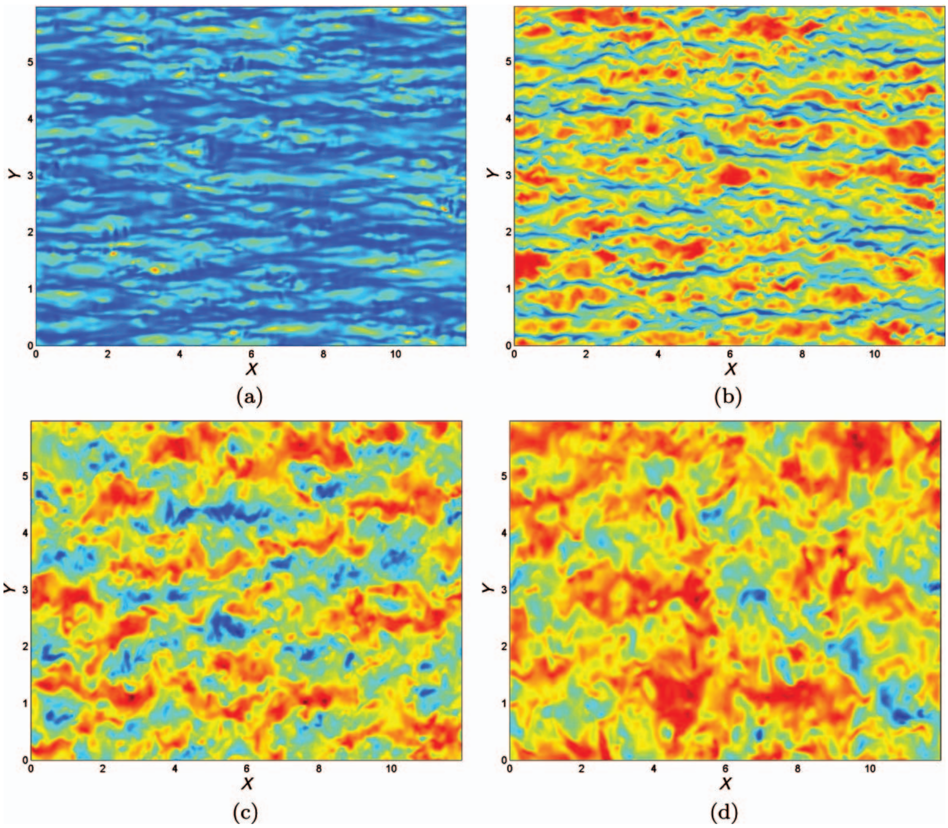

Figure 14. Contours of u at different distances from the wall for $Re_\tau = 360$. Blue denotes negative values and red denotes positive values. (a) $z_+ = 1$, (b) $z_+ = 27$, (c) $z_+ = 160$, (d) $z_+ = 360$.

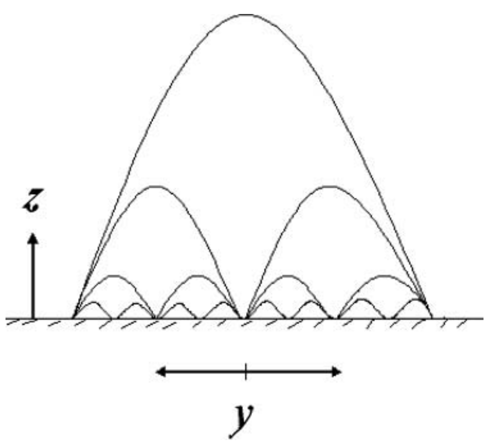

Figure 15. A conceptual sketch of attached eddies of varying distances from the wall.

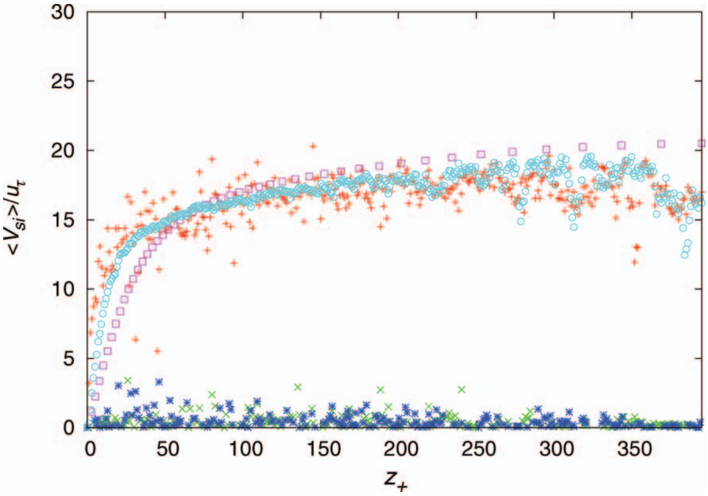

Figure 16. Mean velocities for $Re_\tau = 360$. Red (+) – $\langle \boldsymbol{V}_{sx} \rangle$. Green (x) – $\langle \boldsymbol{V}_{sz} \rangle$. Blue (∗) – $\langle \boldsymbol{V}_{sy} \rangle$. Light blue (○) – $\langle u \rangle_{sp}$. Purple (□) – $\langle u \rangle$.

Hence, the average motion of stagnation points seems to be as if they were fluid elements, but further studies will be needed to sharpen this point as the noise in the statistics presented in Figure 16 remains considerable.

We now turn to the rms, or quadratic mean profiles of the three components of $\boldsymbol{V}_s$. In HIT, the Reynolds number scaling of the variance of $\boldsymbol{V}_s$ is the ratio of the Reynolds number scaling of the variance of the acceleration $\boldsymbol{a}$ (which, in HIT, is the same as the variance of $\boldsymbol{A}$) and of the Reynolds number scaling of the variance of the fluid velocity gradients [7]. This follows from Equation (6), as in HIT, the velocity gradients $\nabla \boldsymbol{u}'$ and $\boldsymbol{V}_s$ are statistically uncorrelated and the acceleration statistics conditional on stagnation points do not show relevant differences from the acceleration statistics collected from the entire flow. In turbulent channel flows, however, $\nabla \boldsymbol{u}'$ and $\boldsymbol{V}_s$ are not uncorrelated. Equation (6) implies that $\langle \boldsymbol{a} \rangle_{sp} = -\langle \boldsymbol{V}_s \cdot \nabla \boldsymbol{u}' \rangle_{sp}$ and we have numerically checked that $\langle \boldsymbol{a} \rangle_{sp}$ does not vanish in the streamwise direction, very much like $\langle \boldsymbol{a} \rangle$. Hence, $\langle \boldsymbol{V}_s \cdot \nabla \boldsymbol{u}' \rangle_{sp}$ is not zero and is also not equal to $\langle \boldsymbol{V}_s \rangle_{sp} \cdot \langle \nabla \boldsymbol{u}' \rangle_{sp}$.

The lack of decorrelation between $\nabla \boldsymbol{u}'$ and $\boldsymbol{V}_s$ in turbulent channel flows means that a full study of these correlations will be needed to understand how the variances of the three components of $\boldsymbol{V}_s$ scale with z_+, the local Reynolds number of the turbulence. This study is too extensive and involved to fit in the present paper, but we do nevertheless motivate it for the future by plotting in Figures 17 and 18, respectively, the z_+-profiles of the rms of $\boldsymbol{V}_s$ and that of $\boldsymbol{a}$ conditional on stagnation points. It is clear that the root mean squares of $\boldsymbol{V}_s$ in all three directions are commensurate with the skin friction velocity u_τ around $z_+ \approx 30$ where they peak, and it is also clear that they decrease with increasing distance from the wall in the region where $z_+ > 30$. This result is significant as it quantifies the fact that, in the local frame of reference moving with the mean stagnation point velocity, the flow topography is most unsteady in the region which might be identified with the buffer layer. The second reason which makes this result significant is its suggestion that, in the limit of very high Reynolds number Re_τ and as one moves away from the wall towards the centre of the channel, the root mean squares of $\boldsymbol{V}_s$ diminish and, presumably, eventually vanish. In this limit the local turbulence becomes approximately homogeneous isotropic

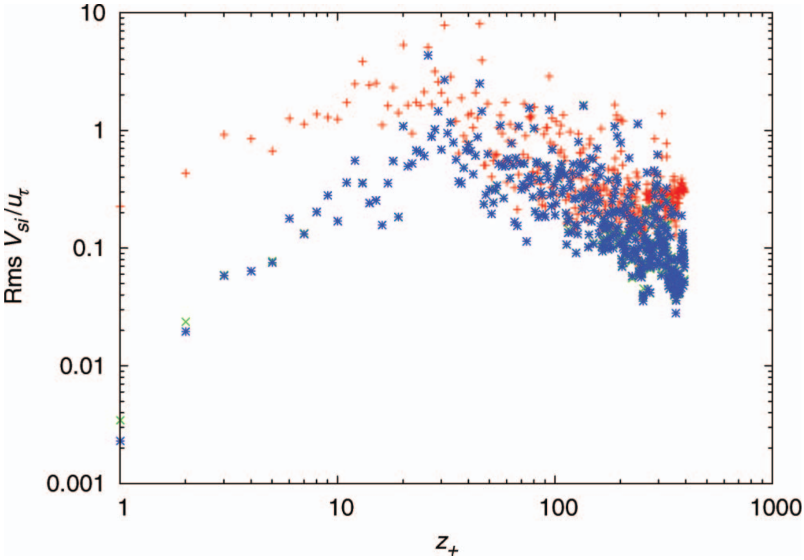

Figure 17. Rms of $\boldsymbol{V}_s$ at stagnation points for $Re_\tau = 360$.

and, as shown by [7], the variance of $\boldsymbol{V}_s$ does indeed tend to 0 as Reynolds number tends to infinity in HIT. Our results therefore seem to be consistent with those of [7].

Figure 18 shows that the variances of $\boldsymbol{a}$ conditional on stagnation points are higher than the unconditional variances of $\boldsymbol{a}$ and that this holds in all three directions. However, it is difficult to conclude much from this figure concerning the differences and/or similarities

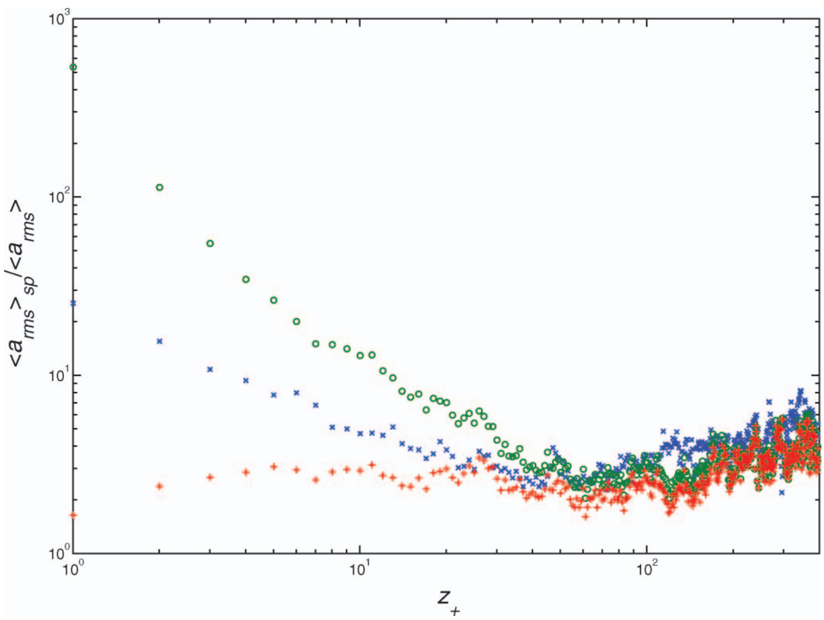

Figure 18. Ratio of $a_{\rm rms}$ at stagnation points and throughout the fluid for $Re_\tau = 360$. Blue (x) – streamwise direction, green (○) – wall-normal, red (+) – spanwise.

between the z_+-profiles of these two variances in the intermediate log-like layer, and it is also impossible to explain Figure 17 from Figure 18 and the statistics of $\nabla \boldsymbol{u}'$. An explanation of Figure 17 will require a study that goes beyond the mean and rms profiles of this paper and considers correlations among accelerations, velocity gradients and stagnation point velocities in some detail. As this is beyond our present scope, we leave it for future study.

8. Conclusions

In turbulent channel flow we are forced to distinguish between the acceleration $\boldsymbol{A}$ corresponding to the full fluid velocity $\boldsymbol{u}$ and the acceleration $\boldsymbol{a}$ corresponding to the fluctuating velocity $\boldsymbol{u}' \equiv \boldsymbol{u} - \langle \boldsymbol{u} \rangle$, where $\langle \boldsymbol{u} \rangle$ is the mean flow. The sweeping decorrelation hypothesis can be adapted to wall turbulence in terms of $\boldsymbol{A}$, if care is taken to recognise that the mean acceleration $\boldsymbol{A}$ is not necessarily zero. This adapted formulation states that the fluctuations of the convective and local parts of $\boldsymbol{A}$ around their means approximately cancel each other in the intermediate log-like layer. This is one of the main results of this paper and is accompanied by our observation that in this same intermediate layer, the fluctuations of $\boldsymbol{a}$ around its mean come predominantly from the fluctuations of its local part, the convective part being negligible by comparison. As the convective part of the acceleration $\boldsymbol{a}$ is by definition zero at stagnation points, we might have expected the fluctuations of $\boldsymbol{a}$ at stagnation points to be representative of the fluctuations of $\boldsymbol{a}$ throughout. However, this is not the case as the variance of $\boldsymbol{a}$ at stagnation points is significantly larger than the unconditional variance of $\boldsymbol{a}$, thus suggesting that the turbulent velocities may be more unsteady around stagnation points than they are in general.

The stagnation points move and their motion is determined by the turbulent velocity gradients and the rate with which the turbulent velocity changes at their location. On average, stagnation points move as if they were fluid elements: The average stagnation point velocity profile coincides with the average fluid velocity profile averaged over the locations of stagnation points. The fluctuations around this average stagnation point motion peak around $z_+ \approx 30$ where they are commensurate with u_τ; they decrease with increasing distance from the wall in the region $z_+ > 30$, and with decreasing distance to the wall in the region $z_+ < 30$.

These results suggest a picture where the topology of the turbulence is just differentially swept, on average, along the channel. This differential sweeping reflects to a significant extent the mean flow profile but is nevertheless different from it. This sweeping picture relates to the sweeping decorrelation hypothesis, which was originally introduced by [19] for HIT and which we reformulate here for wall-bounded turbulence following Tsinober et al.'s [13] explicit formulation in terms of the local and convective parts of the acceleration field.

References

[1] S.B. Pope, *Turbulent Flows*, Cambridge University Press, New York, 2000.
[2] V. Dallas, J.C. Vassilicos, and G.F. Hewitt, *Stagnation point von kármán coefficient*, Phys. Rev. E 80(4) (2009), p. 046306.
[3] A.A. Townsend, *Equilibrium layers and wall turbulence*, J. Fluid Mech. Digital Archive 11(01) (1961), pp. 97–120.
[4] A.A. Townsend, *The Structure of Turbulent Shear Flow*, Cambridge University Press, New York, 1976.
[5] S. Hoyas and J. Jiménez, *Scaling of the velocity fluctuations in turbulent channels up to $Re_\tau = 2003$*, Phys. Fluids 18(1) (2006), p. 011702.

[6] H.E. Fiedler, *Coherent structures in turbulent flows*, Prog. Aerospace Sci. 25(3) (1988), pp. 231–269.
[7] S. Goto, D.R. Osborne, J.C. Vassilicos, and J.D. Haigh, *Acceleration statistics as measures of statistical persistence of streamlines in isotropic turbulence*, Phys. Rev. E 71(1) (2005), p. 015301.
[8] P. Vedula and P.K. Yeung, *Similarity scaling of acceleration and pressure statistics in numerical simulations of isotropic turbulence*, Phys. Fluids 11(5) (1999), pp. 1208–1220.
[9] S.B. Pope, *Lagrangian pdf methods for turbulent flows*, Annu. Rev. Fluid Mech. 26 (1994), pp. 23–63.
[10] B.L. Sawford, *Reynolds number effects in lagrangian stochastic models of turbulent dispersion*, Phys. Fluids A: Fluid Dyns. 3(6) (1991), pp. 1577–1586.
[11] P.K. Yeung and S.B. Pope, *Lagrangian statistics from direct numerical simulations of isotropic turbulence*, J. Fluid Mech. Digital Archive 207 (1989), pp. 531–586.
[12] P.K. Yeung, *One- and two-particle lagrangian acceleration correlations in numerically simulated homogeneous turbulence*, Phys. Fluids 9(10) (1997), pp. 2981–2990.
[13] A. Tsinober, P. Vedula, and P.K. Yeung, *Random taylor hypothesis and the behavior of local and convective accelerations in isotropic turbulence*, Phys. Fluids 13(7) (2001), pp.1974–1984.
[14] A. La Porta, G.A. Voth, A.M. Crawford, J. Alexander, and E. Bodenschatz, *Fluid particle accelerations in fully developed turbulence*, Nature 409 (2001, February), pp. 1017–1019.
[15] N. Mordant, A.M. Crawford, and E. Bodenschatz, *Experimental lagrangian acceleration probability density function measurement*, Phys. D: Nonlinear Phenom. 193(1–4) (2004), pp. 245–251.
[16] J. Mann, S. Ott, J. Berg, and B. Lüthi, *The Correlation Between Velocity and Acceleration in Turbulence*, in *Progress in Turbulence,* II, M. Oberlack, G. Khujadz, S. Günther Weller, Tanja, M. Frewer, J. Peinke, and S. Barth, eds., Springer, Berlin, 2007, p. 95.
[17] R.J. Hill, *Scaling of acceleration in locally isotropic turbulence*, J. Fluid Mech. 452 (2002), pp. 361–370.
[18] G. Gulitski, M. Kholmyansky, W. Kinzelbach, B. Luthi, A. Tsinober, and S. Yorish, *Velocity and temperature derivatives in high-Reynolds-number turbulent flows in the atmospheric surface layer. part 2. Accelerations and related matters*, J. Fluid Mech. 589 (2007), pp. 83–102.
[19] H. Tennekes, *Eulerian and lagrangian time microscales in isotropic turbulence*, J. Fluid Mech. Digital Archive 67(03) (1975), pp. 561–567.
[20] K.T. Christensen and R.J. Adrian, *The velocity and acceleration signatures of small-scale vortices in turbulent channel flow*, J. Turbul. 3 (2002, April), p. 23.
[21] Z. Hu, C.L. Morfey, and N.D. Sandham, *Sound radiation in turbulent channel flows*, J. Fluid Mech. 475 (2003), pp. 269–302.
[22] L. Kleiser and U. Schumann, *Treatment of incompressibility and boundary conditions in 3-D numerical spectral simulations of plane channel flows*, in E.H. Hirschel, ed., *Conference on Numerical Methods in Fluid Mechanics, 3rd, Cologne, West Germany, October 10–12, 1979, Proceedings. (A80-38252 15-34) Braunschweig, Friedr,* Vieweg und Sohn Verlagsgesellschaft mbH, Germany, 1980, pp. 165–173.
[23] J. Kim, P. Moin, and R. Moser, *Turbulence statistics in fully developed channel flow at low Reynolds number*, J. Fluid Mech. Digital Archive 177 (1987), pp. 133–166.
[24] R.A. Antonia and J. Kim, *Low-Reynolds-number effects on near-wall turbulence*, J. Fluid Mech. 276 (1994), pp. 61–80.
[25] H. Abe, H. Kawamura, and Y. Matsuo, *Direct numerical simulation of a fully developed turbulent channel flow with respect to the reynolds number dependence*, J. Fluids Eng. 123(2) (2001), pp. 382–393.
[26] A.E. Perry and M.S. Chong, *On the mechanism of wall turbulence*, J. Fluid Mech. Digital Archive 119 (1982), pp. 173–217.
[27] J. Dávila and J.C. Vassilicos, *Richardson's pair diffusion and the stagnation point structure of turbulence*, Phys. Rev. Lett. 91(14) (2003), p. 144501.
[28] A. Tsinober, *An Informal Conceptual Introduction to Turbulence*, Springer, Berlin, 2009.
[29] W. Heisenberg, *Zur statistischen Theorie der Turbulenz*, Zeitschrift fur Physik 124 (1948), pp. 628–657.
[30] A.M. Yaglom, *On the acceleration field in a turbulent flow*, Dokl. Akad. Nauk SSSR 67(5) (1949), pp. 795–798.